Design, Prototyping, and Characterization of a Micro-Force Sensor Intended for Tissue Assessment in Confined Spaces

Shashank S. Kumat and Panos S. Shiakolas

Abstract—The quantitative characterization of soft tissue viscoelastic properties can aid in disease prognosis and diagnosis. Existing technologies present challenges to measuring localized in vivo tissue relaxation data while meeting load and geometric constraints. This research presents the design, prototype, and characterization of a micro-force sensor that could enable better access to confined spaces of the human body. The novel design of the uniaxial micro-force sensor has an external diameter of less than or equal to 3.5 mm and 1 N load capacity for transurethral palpation of the bladder interior wall. The conceptual design of the micro-force sensor and a finite element-based discrete optimization procedure to determine the optimum values of the identified design parameters of bend radius, bend angle, and thickness while meeting defined operational and geometric constraints are presented. These optimum values guided the prototyping of an aluminum sensing element with 2.18 mm bend radius, 104.9° bend angle, and 0.3 mm thickness. A miniature metal foil strain gauge was attached at defined location on the sensing element for measurement purposes. An experimental testbed was developed, calibrated, and used for characterization experiments. The performance matrix of the prototyped micro-force sensor was experimentally evaluated. The sensitivity, resolution, accuracy, precision, and repeatability band of the sensor were evaluated to be 859.73 $\mu\epsilon$/N, 2.6 mN, 28.6 mN, 87.22%, and ±2.87%, respectively, with a hysteresis of 118 mN. These experimental results provide confidence to further employ the sensor for in vivo experiments toward the identification of viscoelastic properties of soft tissue.
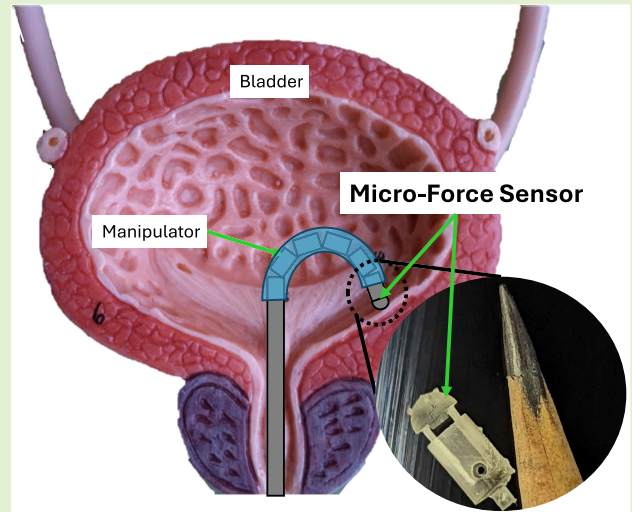
Index Terms—Finite element analysis, force sensor performance, micro-force sensor, strain gauge.

I. INTRODUCTION

MEDICINE has long used tissue palpation, a subjective technique, for assessing the health of an organ [1], [2], [3], [4], [5]. During diagnosis, manual palpation and indentation techniques have been employed to categorize abnormal tissue of the bladder, prostate, breasts, and anterior vaginal wall [6], [7], [8], [9]. Using controlled tissue indentation to obtain quantitative force relaxation feedback can be a valuable diagnostic method to assist with disease prognosis [1], [10], [11], [12], [13].

Researchers have been investigating and developing sensors for biomedical applications while attempting to meet the required performance specifications for each application. Tanimoto et al. [14] developed a force feedback sensor for neurosurgery (1.6 mm diameter, 12 mm length, 29 mN load capacity). Shin et al. [15] designed a fiber optic-based cardiac ablation sensor (2.3 mm diameter, 0.5 N load, 1 mN resolution). Alekya et al. [16] investigated a diaphragm-based tissue sensor (3.5 × 3.5 × 0.5 mm, 0–250 mN range). Along with challenges in miniaturization, these sensors cannot be used to evaluate tissue viscoelastic properties for confined space applications since loads in the range of 0.2–1.2 N are required for effective characterization [9], [17], [18], [19], [20].

Fiber optic or optical-based sensors for surgical applications have also been investigated. Yip et al. [21] developed a micro-force sensor for mitral valve annuloplasty (5.5 mm diameter, 12.0 mm length, 4 N force). Puangmali et al. [22] proposed a laparoscopic sensor (5 mm diameter, ±3 N axial force,

20 mN resolution). Luo et al. [23] created a ureteroscopic sensor (2 mm diameter, 14.5 mm length, 20 mN resolution, 10 N axial load). Yip et al. [21] linked sensor sensitivity to fiber bending, cautioning against small bend radii. Fiber optic sensors faced challenges in confined spaces such as the bladder with routing and manipulating, which lead to poor repeatability [21], [24].

The dimensions of medical diagnostic devices need to be defined considering reported anatomical measurements. The average diameter with a maximum stretch of the external urethral meatus was reported to be within the range of 6.0–10.3 mm [25], [26], [27]. The outside diameter of a commonly used flexible endoscope is between 5.0 and 8.3 mm [28]. Hudson et al. [28] performed a study involving 115 patients (60 male and 55 female) to examine the impact of flexible ureteroscope (FU) diameter on the ease of passage. They found that decreasing the diameter of the FU from 9.0 to 7.4 Fr (3.00–2.47 mm) resulted in a significant decrease from 37% to just 0.9% in failed insertion attempts. Miernik et al. [29] investigated the occurrence of urethral wall injuries in association with the size of the instruments used during ureteroscopy on 153 patients (114 male and 39 female). They reported that, after using instruments with diameter from 14.0 to 16.0 Fr (4.67–5.33 mm), superficial lesions on the urethra walls were observed in approximately 39.9% of the patients, deeper lesions were present in approximately 17.6%, and circumferential perforation was found in approximately 47.7% of the individuals. A study by Lildal et al. [30] involving 180 patients (110 male and 70 female) reported that the incidence of lesions and complications associated with post-ureteroscopic surgery decreased significantly when smaller diameter ureteroscopy instruments were used, specifically those ranging from 10.0 to 12.0 Fr (3.33–4.00 mm) in size.

These studies strongly support the notion that reduced-diameter transurethral instruments directly correlates with minimizing and reducing patient trauma. Although several researchers attempted to construct diagnostic devices to quantitatively record data toward evaluating tissue viscoelastic properties in vivo, they have not been successful in meeting necessary design specifications toward reducing patient trauma, tissue damage, and lesions while accessing organs through a natural orifice [5], [10], [14], [16], [18], [20], [21], [22], [23], [31], [32].

Rigid link manipulators have limited capability to interrogate the entire bladder through contact palpation, as such a ten-joint six-degree of freedom compliant manipulator was proposed to access the "difficult-to-reach" areas within the bladder including the trigone [33]. Adejokun and Shiakolas [33] and Adejokun et al. [34], [35] presented a compliant robotic manipulator for bladder contact palpation through the urethra with an overall diameter of 4 mm. The sensor presented in this research is envisioned to be attached at the tip of the manipulator proposed by Adejokun et al. [35]. The manipulator and attached sensor system could be used to access the bladder to palpate and interrogate any region of the bladder interior wall with appropriate load capacity while recording the tissue reaction and relaxation forces.

As such, there is a need for a system capable of accessing confined spaces in the human body through a natural orifice to interrogate the tissue surface under consideration with an appropriate force range and resolution for meaningful measurements while substantially reducing patient trauma and discomfort during the procedure. Such a system must easily function in a clinical setting where measurements could be performed at regular time intervals as prescribed by the physician.

The micro-force sensor proposed and investigated in this research could be employed for diagnostic applications such as transurethral palpation or palpation during minimally invasive surgical interventions [15], [18], [21], [22], [23].

The work presented in this research introduces the conceptual design, structural design, and optimization of a novel uniaxial micro-force sensor aimed to address issues identified with existing sensors and their application to transurethral palpation of the internal bladder wall tissue for medical diagnostic purposes. The manuscript also discusses the procedures for the fabrication and presents the experimentally characterized performance matrix of the sensor.

This research article presents the conceptual design (Section II) of the micro-force sensor and its components. Section II-B discusses the design optimization formulation along with the design constraints and bounds on the design parameters. Section II-C introduces an automated finite element-based exhaustive search algorithm to identify optimal design parameters. Section III discusses the fabrication of a functional prototype of the micro-force sensor. Subsequently, Section IV describes the experimental testbed and its use to evaluate the performance characteristics (sensitivity, resolution, accuracy, precision, repeatability, and hysteresis) of the micro-force sensor. The manuscript concludes with a summary of the results and proposes future investigation.

II. DESIGN OF SENSOR

A. Conceptual Design

The solid model of the micro-force sensor concept, presented in Fig. 1, consists of three major components: sensor head, sensor base, and sensing element. The sensor base component is intended to be attached to the manipulator researched by Adejokun and Shiakolas [33] and Adejokun et al. [34], [35].

When the manipulator palpates the target tissue, the sensor head will translate along the loading axis (global Y-axis) and engage with the sensing element at location D as presented in Fig. 1. The load acting on the sensor head will be transferred to and generate a strain on the sensing element (since location A of the sensing element is fixed on the sensor base). The sensing element must withstand the maximum applied load without undergoing plastic deformation while meeting space constraints. The measurements based on the sensing element deformation must also meet a desired operational resolution and exhibit linear behavior in its range of operation.

Furthermore, micro-force sensors for confined space applications such as the human bladder must consider their size as it relates to ease of access through the urethra (reduce patient trauma and tissue lesions), the range of normal force to be applied at the tip of the sensor, and the operational
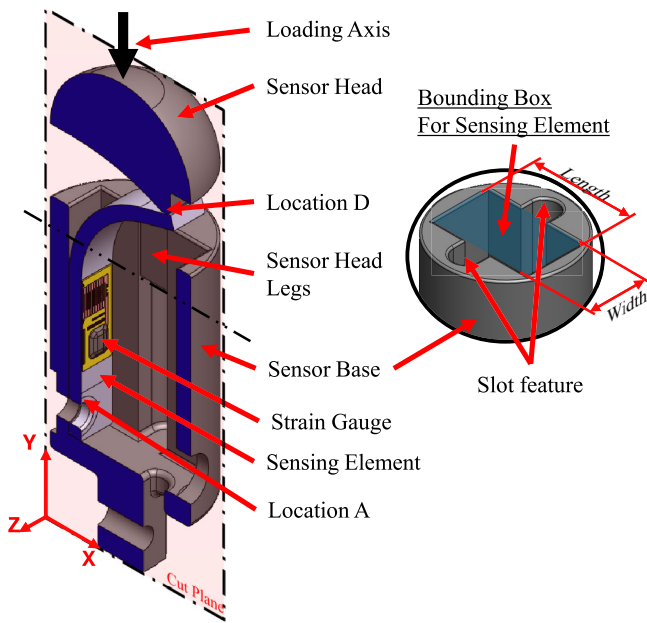
Fig. 1. Initial sensor design concept section view, showing sensor head, sensing element, strain gauge, and sensor base components.

TABLE I
MICRO-FORCE SENSOR DESIGN SPECIFICATIONS

Characteristic	Specification
Diameter	≤3.5 mm (sensor housing)
Force Range	≤1.0 N (normal force)
Resolution	20 mN
Accuracy	± 30mN
Safety Factor	≥ 3.5
Operating environment	Wet/Moist
Other	Biocompatibility

environment conditions. The desired specifications for the micro-force sensor to meet the operational requirements of tissue palpation primarily in the confined space of the bladder are presented in Table I.

A miniature metal foil strain gauge will be attached on the sensing element to measure the strain experienced by the sensing element and as such it must meet dimensional constraints and operational performance requirements. Since the overall diameter of the sensor needs to be less or equal to 3.5 mm, the size of an imaginary bounding box or space where the sensing element will reside (refer to Fig. 1) is defined to be 5 × 1.55 × 2.7 mm (height × width × length). Further increasing the length and/or width of the bounding box will require an increase in the overall diameter of the micro-force sensor.

A miniature metal foil strain gauge (N2K-06-S5024G-50C/DG/E5, Micro-Measurements Inc., Wendell, NC, USA) with total packing planar dimensions 1.9 × 1.4 mm satisfies the bounding box constraints and will be used in this research. The dimensions of the strain gauge impose additional constraints to the design parameters of the sensing element. The linear operating range of this strain gauge is ±3000 $\mu\epsilon$ which adds another requirement relating to its placement on
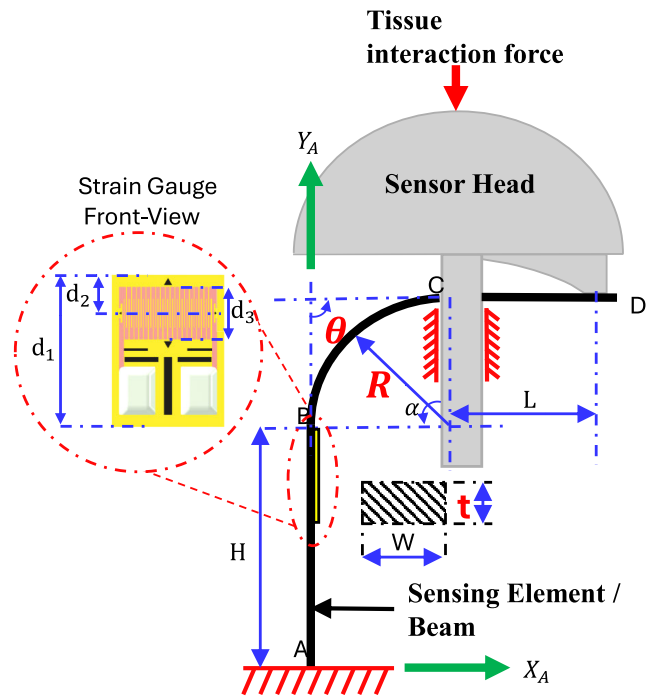

Fig. 2. Drawing of the initial design concept of the sensing element showing the design parameters along with expected loading conditions.

a flat surface of the sensing element. The critical parameters affecting the strain experienced by the sensing element must be identified and designed for.

B. Design Optimization Problem Formulation

A drawing of the initial micro-force sensor concept is presented in Fig. 2.

The critical design parameters of the sensing element were identified and analyzed to maximize the absolute strain evaluated at the desired strain gauge attachment location in order to improve the sensitivity, resolution, and operating load range of the sensor. Since the strain gauge must be attached on a flat surface, the preferred location will be along AB as shown in Fig. 2. The height H, the length of segment AB, (refer Fig. 2) must be at least 1.9 mm, which is the length of the strain gauge packing. In addition, for fabrication of the active height of the sensing element, a provision for a mounting hole to attach the sensing element to the sensor base needs to be considered, which requires the total fabricated height to be at least 3.9 mm. The sensing element design parameters as shown in Fig. 2 are the radius of curvature R, the bend angle relative to the vertical member of the beam θ, and the thickness of the beam t.

The optimization formulation is presented in (1), where $\gamma_b(R, \theta, t)$ is the normal (Y-axis) strain evaluated at the desired location, γ_{sg} is the linear operating limit of the strain gauge, σ_{max} is the maximum von Mises stress experienced by the sensing element during loading, S_y is the yield strength of the sensing element material, and N_f is the factor of safety. This sensor is intended to be attached on and be an integral component of a medical diagnostic device and as such, the

factor of safety is defined to be 3.50

Max: $|\gamma_b(R, \theta, t)| \quad [\mu\epsilon]$

Such that:
$$\begin{cases} \sigma_{\max} \times N_f \leq S_y & [\text{MPa}] \\ R(1 + \cos\theta) + L\sin\theta + (t/2) \leq 2.5 & [\text{mm}] \\ H + R\sin\theta - L\cos\theta \leq 6.5 & [\text{mm}] \\ \gamma_{sg} - |\gamma_b(R, \theta, t)| \geq 0 & [\mu\epsilon] \end{cases}$$

Limits:
$$\begin{cases} 0.2 \leq t \leq 0.35 & [\text{mm}] \\ 0.2 \leq R \leq 3.7 & [\text{mm}] \\ 90 \leq \theta \leq 130 & [\text{deg}]. \end{cases} \quad (1)$$

The objective of the optimization formulation is to maximize the strain at the desired location on the sensing element while satisfying the defined constraints. It is important to note that the sensitivity of the sensor is directly related to the strain and as such maximizing the strain will improve the sensitivity and resolution of the proposed device while satisfying the operational and geometric constraints. However, the strain must remain in the linear operating range of the strain gauge of $\pm 3000\ \mu\epsilon$, and the sensing material should not experience any plastic deformation.

The optimization formulation must also consider the positioning of the central location of the active length of the strain gauge on the sensing element based on the characteristic dimensions of the identified miniature strain gauge. These dimensions, provided by the manufacturer, are shown in Fig. 2, where $d_1 = 1.99$ mm is the total length of the gauge packing, $d_2 = 0.48$ mm is the distance from the top of the packing to the center of the active length, and $d_3 = 0.66$ mm is the active length of the gauge. The dimensions of the strain gauge are used to define the attachment location of its central axis at 0.48 mm from B toward A (refer Fig. 2).

The optimization formulation includes inequality constraints for the allowable stress while geometric constraints are imposed on the overall dimensions of the sensing element. An inequality constraint is added to ensure that the estimated strain on the sensing element does not exceed the operating range of the strain gauge. The upper and lower bounds of the design parameters are defined using different criteria including geometric limitations, machinability, manufacturability, ease of assembly, improved sensitivity, and off-the-shelf component availability.

The location of the contact point D along the bending element arm, CD, changes dynamically depending on the magnitude of the applied force, and it is a function of (R, θ, L, t). This dynamic dependency causes the behavior of the bending element arm to be a nonlinear function of the sensor head displacement.

A unique combination of values of the design parameters of the sensing element is defined as a design point. These parameters, their range, and discretization levels are the bend radius $R \in [0.2, 3.7]$ mm in increments of 0.5 mm for eight values, the bend angle $\theta \in [90°, 130°]$ in increments of 10° for five values, and the thickness $t \in [0.2, 0.35]$ mm in increments of 0.05 mm for four values. This discretization yields a total of 160 unique design points. Out of the 160 possible design points, 31 were discarded since they did not meet the desired

bounding box constraint (see (1) and Fig. 1). The remaining 129 design points, called feasible design points, were analyzed using parametric FE analysis. The proposed sensor will be covered with a biocompatible sheath; thus, addressing the operating environment specification and at the same time allow for the use of non-biocompatible materials. In this work, aluminum (Al-6061-T6) was selected for the sensing element.

C. Finite Element Analysis

The feature of the sensor head interacting with the sensing element was modeled to automatically align at the desired interaction location (location D in Fig. 2) on the sensing element through the geometric constraints presented in (1). The design parameters of the feasible design points were parameterized in SolidWorks (Dassault Systemes, Waltham, MA, USA), a computer-aided design (CAD) modeling software. The solid model was then imported into the FE software ANSYS (Canonsburg, PA, USA) Workbench R21.1. The imported CAD model was further processed to automate the exhaustive search discrete optimization procedure by defining the design parameters in Ansys DesignModeler R21.1.

A planar symmetry boundary condition was advantageously employed [refer Fig. 3(a)] to reduce computation time for the FE analysis. The FE model of the sensing element was preprocessed to obtain targeted and localized solutions. The interaction between the slots of the sensor base and the legs of the sensor head was also modeled by defining frictional contact between them.

The complex features of the sensor head and base components were fabricated using additive manufacturing [17]. The Formlabs gray resin material properties were used for the structural analysis (Formlabs Inc., Somerville, MA, USA). The material properties of aluminum were assigned to the sensing element. The analysis for a single design point was performed by setting the boundary conditions of the model according to Fig. 3(b).

The FE model mesh was generated using 10-node tetrahedral and 20-node hexahedral elements. These elements improve the convergence rate since they offer robust adaptivity during mesh refinement and could obtain higher solution accuracy due to their ability to handle complex geometric features for a computationally efficient solution [36]. The adaptive mesh control process automatically iterates and refines the mesh density until either the convergence criterion (1%) or the maximum number of refinement loops is met. A representative FE mesh is shown in Fig. 3(c).

The sensor is expected to sense normal palpation reaction loads up to 1 N. This load is used for design purposes to estimate the maximum strain, stress, and safety factor of the sensing element. The load applied on the top surface of the sensor head during FE analysis is 0.5 N due to model symmetry as shown in Fig. 3(b).

The normal strain along the Y-axis was evaluated at 0.48 mm below the starting point of the bend indicated as "Top strain probe" in Fig. 4(a). This location was selected considering the central axis of the active length of the
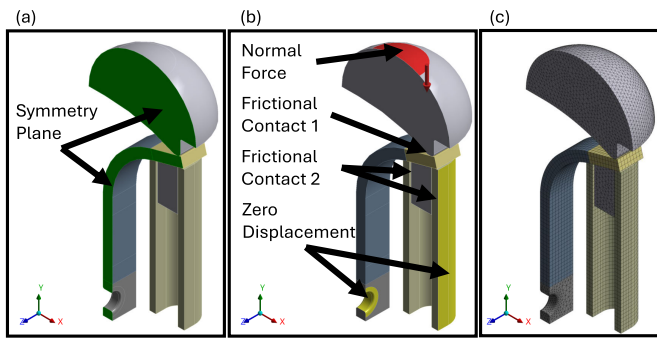
Fig. 3. Finite element-based model (a) section view and the surface of symmetry, (b) applied boundary conditions and friction contact region, (c) generated mesh.
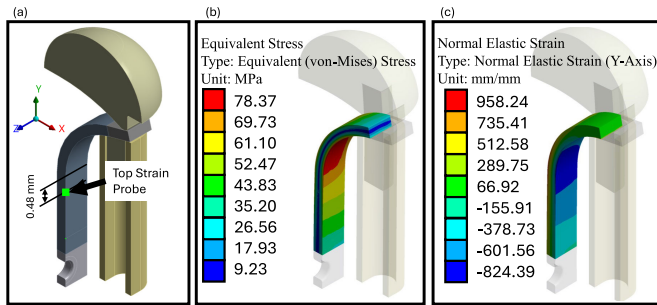

Fig. 4. Finite element-based model due to maximum applied load of 0.5 N, (a) location for strain evaluation, (b) von Mises stress contour for the beam element with design parameters set to (R, θ, t) = (2.2 mm, 110°, 0.3 mm), and (c) normal elastic strain distribution along the global Y-axis.

identified strain gauge with respect to its packing as discussed in Section II-B.

The von Mises stress was evaluated for the targeted region of the sensing element. Fig. 4(b) shows the results of the von Mises stress distribution due to the maximum loading condition for a design point with design parameters bend radius, bend angle, and thickness of 2.2 mm, 110°, and 0.3 mm, respectively. Fig. 4(b) shows that the maximum stress occurs at the bend of the sensing element. Similar stress contours were observed for all design points. The maximum von Mises stress for each design point was used to evaluate the respective safety factor [37].

For example, a safety factor $N_f = 3.6$ is achieved for the results presented in Fig. 4(b), where the maximum von Mises stress was evaluated as $\sigma_{\max} = 78.37$ MPa with the yield strength of the sensing element material (Al-6061-T6) being $S_y = 280$ MPa. Fig. 4(c) presents the strain distribution for the same design point (R = 2.2 mm, θ = 110°, $t = 0.3$ mm) due to the maximum applied loading condition. The strain distribution contour helps to identify the location for the central axis of the active length of the strain gauge. Furthermore, it can be deduced from Fig. 4(c) that the maximum compressive strain was found near the "Top strain probe," indicating that the active surface of the strain gauge must be positioned near this location to obtain improved sensitivity. The strain evaluated at the top strain probe and the von Mises stress due to maximum loading conditions are set as output parameters of the FE analysis. The results from
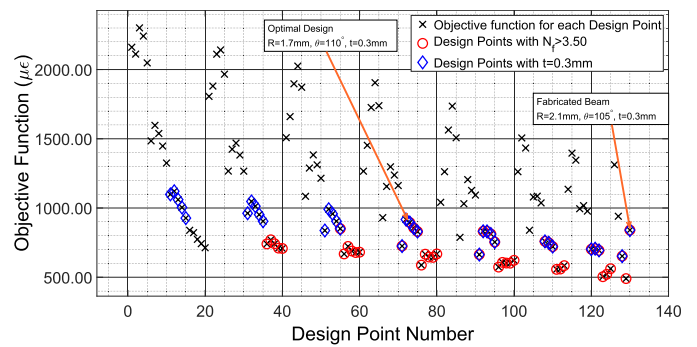

Fig. 5. Cost of the objective function evaluated for the 129 design points along with the one for the manufactured sensing element; the overlaying circle represents the designs with a safety factor greater than 3.5.

the parametric FE analysis are post-processed to identify the optimal design parameters of the sensing element.

D. Optimal Design

The goal of this step in the design process was to identify the geometric parameters which maximize the cost of the objective function (absolute value strain at the "Top strain probe") while satisfying all constraints. The cost of the objective function evaluated for the 129 feasible discrete design points is plotted in Fig. 5. The cross (×) represents the cost of the objective function for all the feasible discrete design points. The circle (○) represents the subset of design points exhibiting a factor of safety greater than 3.50. The diamond (◇) represents the subset of design points with a beam thickness of 0.3 mm. All designs with beam thickness less than or equal to 0.25 mm exhibited a factor of safety less than 3.5, and these design points were not considered for further analysis.

Design point 73 is the optimal design point identified through the optimization analysis based on the discrete values of the design parameters while satisfying all the defined constraints. The optimal design point (point 73) has a bend radius of 1.7 mm, a bend angle of 110°, and a beam thickness of 0.3 mm yielding an objective function cost and safety factor of 894.98 $\mu\epsilon$ and 3.54, respectively. Design point 130 is the cost of the objective function evaluated by using the measured dimensions of the fabricated sensing element (further discussion provided in Section III) in the FE model. This design point yields a cost of 840.55 $\mu\epsilon$ and a safety factor of 3.74.

Fig. 6 presents the effect of bend radius and bend angle on the objective function when the beam thickness is set to 0.3 mm for the 32 feasible design points. As the bend angle increases from 90° to 100°, the cost of the objective function increases for all bend radii. However, further increasing the bend angle reduces the cost of the objective function. The optimal design point in Fig. 6 is shown along the 110°-bend angle with a bend radius of 1.7 mm and cost function of 894.98 $\mu\epsilon$.

It is observed that if the bend radius is 2.2 mm or more, then all feasible design points yield safe designs. This observation could prove useful during fabrication of the sensing element considering manufacturing constraints.
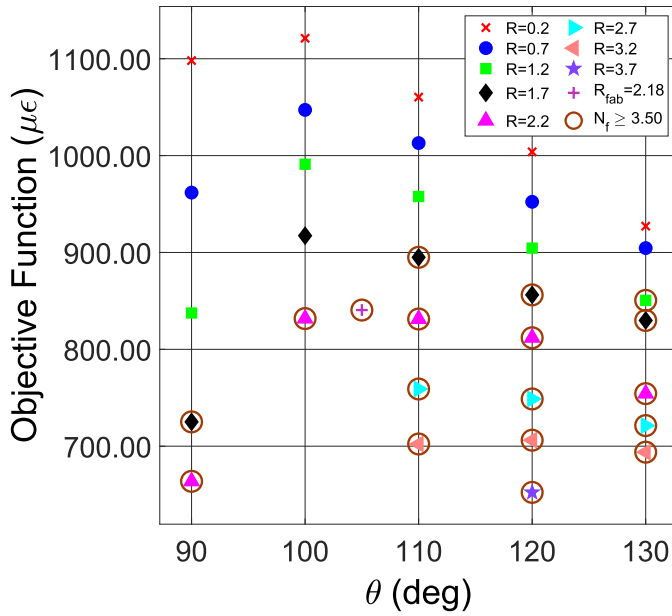
Fig. 6. Effect of bend radius and bend angle for a thickness of 0.3 mm sensing element for an applied load of 0.5 N on the cost of the objective function along with the cost of the objective function of the sensing element using fabricated dimensions all using FE analysis.

III. FABRICATION OF THE MICRO-FORCE SENSOR

A 0.3-mm thick aluminum sheet was used to fabricate the sensing element. An off-the-shelf $\phi 4.00$ mm dowel pin will generate a bend radius of 2.15 mm at the neutral axis for a 0.3-mm thick aluminum sheet. According to FE-based analysis, a bend radius of 2.15 mm yields a safe design with an objective function of 833.40 $\mu\epsilon$ when the bend angle is 100°. A three-point bend press with an off-the-shelf 90° die was used to bend the aluminum sheet, which will experience spring back after bending. These specifications and conditions, even though not the optimal ones, were selected for the fabrication of the sensing element considering available fabrication resources.

The spring back affects the final bend radius R_f (mm), which can be calculated according to (2). The spring back is a function of the initial bend radius R_i (mm), the material properties of yield strength S_y (MPa) and modulus of elasticity E (MPa), and the thickness t (mm) of the sheet metal [38]

$$R_f = \left[4\left(\frac{R_i S_y}{Et}\right)^3 - 3\left(\frac{R_i S_y}{Et}\right) + 1 \right]^{-1} \cdot R_i. \quad (2)$$

The length of the neutral axis of a curved member, L_b, also called bend allowance, is a function of the inner bend angle α (rad), bend radius R (mm), thickness of the sheet metal t (mm), and spring back factor k ($k = 0.5$ for $R > 2t$), as shown in (3) [38]. Since the length of the neutral axis remains the same before and after elastic bending [37], the final inner bend angle α_f (rad) is calculated as a function of the initial inner bend angle α_i (rad) according to (4)

$$L_b = (R_i + kt) \cdot \alpha_i = (R_f + kt) \cdot \alpha_f \quad (3)$$

$$\alpha_f = \frac{R_i + kt}{R_f + kt} \cdot \alpha_i. \quad (4)$$

An expression for the final bend angle θ_f is obtained by combining (3) and (4) to yield as follows:

$$\theta_f = \pi - \alpha_f = \pi - \left(\frac{R_i + kt}{\frac{R_i}{4\left(\frac{R_i S_y}{Et}\right)^3 - 3\left(\frac{R_i S_y}{Et}\right) + 1} + kt} \right) \cdot \alpha_i. \quad (5)$$

Using (5), the final bend angle of the sensing element due to spring back is calculated to be $\theta_f = 97°$ when the initial bend angle $\theta_i = 90°$ and the initial bend radius $R_i = 2.15$ mm for aluminum with yield strength $S_y = 280$ MPa and modulus of elasticity $E = 68.9$ GPa.

The fabricated sensing element design parameters were found to be an inner radius $R_{f\text{-fab}} = 2.03$ mm, a neutral axis bend radius $R_{\text{neutral-fab}} = 2.18$ mm, a bend angle $\theta_{f\text{-fab}} = 104.9°$, and a thickness $t_{\text{fab}} = 0.3$ mm. These parameters were used to perform an FE analysis with a load of 0.5 N (using the symmetric model) yielding an objective function cost $\gamma_b(R_{f\text{-fab}}, \theta_{f\text{-fab}}, t_{\text{fab}}) = 840.55$ $\mu\epsilon$ and factor of safety $N_f = 3.74(>3.5)$. These results are shown in Fig. 6 with the plus symbol (+).

The sensor housing subsystem was prototyped using additive manufacturing technology (low force inverted vat photopolymerization). The external diameter of the prototype sensor housing or base used in this work is 3.3 mm [17].

IV. MICRO-FORCE SENSOR CHARACTERIZATION

The assembled sensor was calibrated and then its performance matrix developed. The performance matrix is based on post-processing the measurements from the sensor characterization experiments. Results from characterization experiments were compared with those obtained from the FE analysis.

The developed experimental testbed is shown in Fig. 7. The sensor-attached fixture mounted on the linear actuator was initially adjusted to a relative no-load state. A precision miniature translational stage (MM-4M-EX, National Aperture Inc., Salem, NH, USA) with an accuracy of ±2 μm was used for the controllable displacement of the micro-force sensor. A custom control and data acquisition program was created in LabVIEW (National Instruments Inc., Austin, TX, USA) to control the dc servo motor driving the linear actuator using an NI myRIO microcontroller.

An SMT series (4501017/B, MTS[1], Eden Prairie, MN, USA) load cell was calibrated using dead weights and then used to measure the reaction load from the sensor during controlled displacement loading of the micro-force sensor.

The signals generated by the sensor and the load cell were acquired by a 24-bit National Instruments, NI-9219 data acquisition module (DAQ), mounted on an NI-9174 chassis connected to a computer running National Instruments LabVIEW software via USB connection. LabVIEW was programed to acquire the load experienced by the calibrated load cell in Newton (N). A four-wire resistance measurement approach was implemented to measure the resistance of the strain gauge. The nominal resistance of the strain gauge after attached on the beam was recorded to be $R_{\text{sg}} = 4995.04$
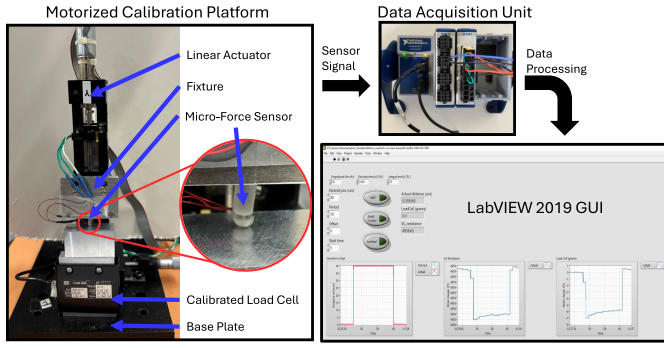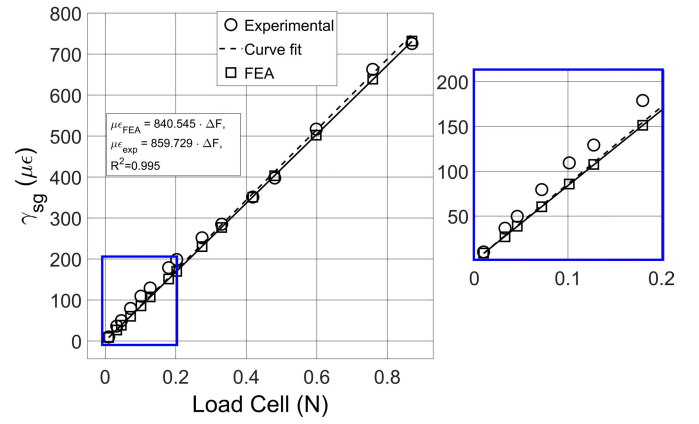
---

[1]Registered trademark.

Fig. 7. Sensor calibration platform.

Fig. 8. Sensitivity responses for the FE-based simulation and experimental data as a function of force experienced by the load cell.

Ω. A 24-bit DAQ device discretizes a 10 KΩ (automatically selected range based on the nominal strain gauge resistance according to DAQ manual) into 1.19 mΩ discrete steps $(10\,000/2^{23})$ [39]. The equivalent strain γ_{sg} can be calculated as a function of the change in resistance ΔR_{sg}, the gauge nominal resistance R_{sg}, and the gauge factor K_{sg}, according to (6) [40]. The gauge factor of the selected miniature foil strain gauge is $K_{sg} = 2.03$

$$\gamma_{sg} = \frac{1}{K_{sg}} \frac{\Delta R_{sg}}{R_{sg}}. \tag{6}$$

The sensor characterization setup presented in Fig. 7 was used to perform the calibration experiments in an automated manner.

The sensor characterization procedure was performed through randomized ordered loading and unloading experiments in triplicates with a single factor (applied displacement) at 15 distinct levels ranging from 21 to 315 μm at an interval of 21 μm. The experimental results were post-processed to evaluate the sensitivity, resolution, accuracy, precision, repeatability, and hysteresis of the sensor.

A. Sensitivity

Sensitivity is the ability of the sensor to capture the change in output variable for a given change in input variable [41]. Therefore, the sensitivity of the micro-force sensor is the change in resistance due to change in applied force, which relates to the controlled displacement of the linear actuator.

During the characterization experiments, the change in load from the calibrated load cell and the change in resistance from the strain gauge attached micro-force sensor were recorded. The calibration equation of the micro-force sensor is shown in (7), where $K_{sg} = 2.03$ is the gauge factor provided by the manufacturer, ΔR_{sg} is the measured change in resistance, $R_{sg} = 4995.04$ Ω is the measured no-load nominal resistance after attached on the sensing element, C_0 is the calibration factor, and ΔF is the force experienced by the micro-force sensor, which is measured by the load cell

$$\gamma_{sg} = \frac{1}{K_{sg}} \frac{\Delta R_{sg}}{R_{sg}} = C_0 \cdot \Delta F. \tag{7}$$

The experimental and FE-based sensor calibration factors were found to be $C_{0-exp} = 859.7$ $\mu\epsilon$/N (8.71 Ω/N) and $C_{0-FE} = 840.55$ $\mu\epsilon$/N (8.52 Ω/N), respectively, with the

sensitivity plots presented in Fig. 8. The calibration analysis shows an excellent linear behavior with a coefficient of determination $R^2 = 0.99$ between the strain gauge sensor and the load experienced by the load cell. This result further confirms that the force on the sensor head can be accurately monitored and measured.

B. Resolution

The resolution of the micro-force sensor system is its ability to detect the smallest measurable change in the strain gauge resistance assuming the sensing element material is in its elastic range and the attached strain gauge in its linear operating range. As discussed by Ahmad et al. [42], the desired resolution bit for analog to digital converter (ADC) can be obtained using the following equation:

$$\text{bitADC} = \log_2 \frac{\text{Force Range}}{\text{Resolution}} + 1. \tag{8}$$

According to Table I, the desired force range and resolution are 1 N and 20 mN, respectively, which according to (8) yield a desired bitADC = 6.64. This bitADC value is well within the capabilities of the selected 24-bit DAQ device at 100 Hz sampling rate.

As established in Section IV, the resolution of a 24-bit data acquisition system allows for the measurement of a change in the resistance of the strain gauge of 1.19 mΩ, which corresponds to an equivalent load change of 0.13 mN using the experimental calibration (7).

A no-load experiment was performed and the steady-state response (approximately 10 min) at 100 Hz sampling rate was analyzed. The difference of the measured values for the resistance of the strain gauge during this time span was evaluated to be ± 10 mΩ relative to the initial no-load resistance. This difference yields $\Delta R = 20$ mΩ, which, according to (7), corresponds to a force resolution of 2.3 mN. This force resolution is smaller than the desired resolution of 20 mN.

C. Accuracy

The accuracy of the sensor could be evaluated as the deviation of a measured quantity from the load experienced
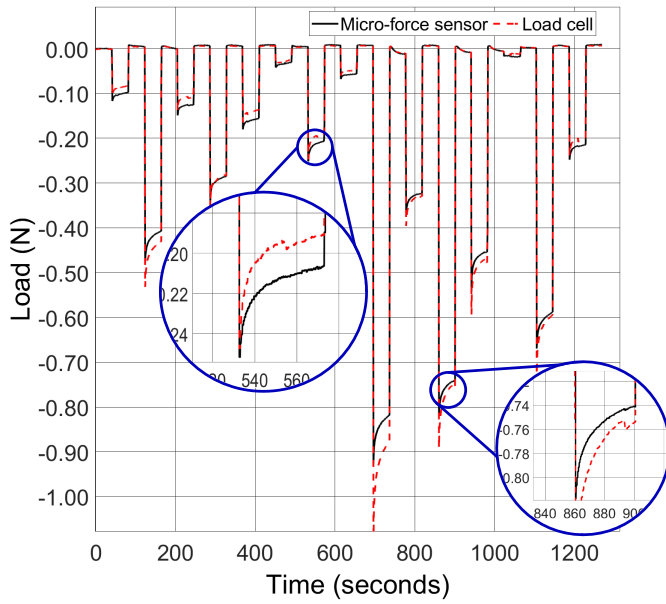
Fig. 9. Load cell and post-processed micro-force sensor data as a time series plot (negative values indicate compressive loads).

Fig. 10. Evaluated force time history from measured ΔR_{SG} for the same controlled applied displacement in triplicate.

by the load cell [41] or as full-scale output, %FSO [43]. The accuracy values to be evaluated depend on the specifications of the currently used equipment such as the microactuator positioning of ± 2 μm and the load cell resolution of 9.80 mN (1.0 g).

Fig. 9 presents the raw data collected from the load cell and the post-processed data from the strain gauge attached micro-force sensor for a single experiment. Similar behavior was observed for the other two experiments.

The accuracy of the micro-force sensor is evaluated as the force root mean square error, F_{RMSE}, according to (9), where, F_{mfs} is the micro-force sensor load calculated by rearranging the calibration (7), F_{LC} is the actual load measured from the load cell, i is the experiment run number, and n is the total number of experiments performed [18]

$$F_{RMSE} = \sqrt{\frac{1}{n}\sum_{i=1}^{n}\left(F_{mfs,i} - F_{LC,i}\right)^2}. \quad (9)$$

The accuracy is also evaluated using the same data as %FSO according to (10), where FSR is the full-scale range of the sensor [43]. The micro-force sensor FSR is 0.87 N

$$\%FSO = \frac{\left|F_{mfs,i} - F_{LC,i}\right|}{FSR}100\%. \quad (10)$$

The analysis of the three measurement sets yields $F_{RMSE} = \pm 28.6$ mN ($\sim\pm 2.92$ g). The %FSO accuracy is also evaluated for each measurement and found to have a maximum value of 3.7%, which corresponds to 29 mN (~ 2.95 g). The accuracy values evaluated by the two approaches differ by 0.4 mN (~ 0.03 g) and both values are less than the desired accuracy of ± 30 mN.

D. Precision

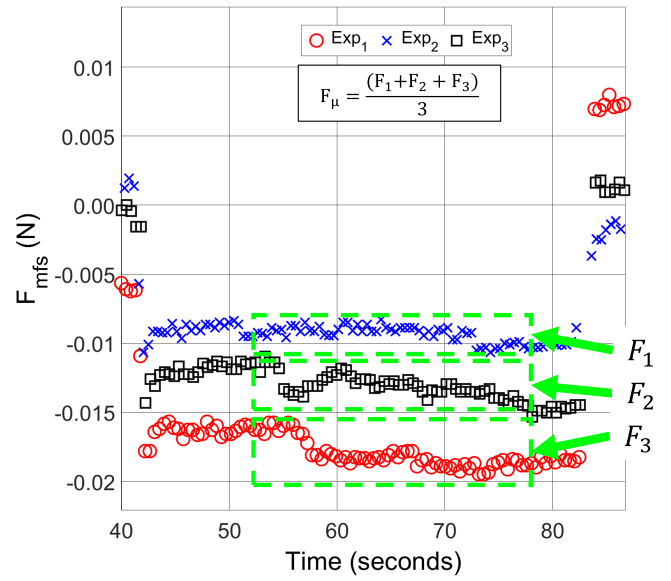Precision refers to how closely individual measurements are in agreement with each other over a particular loading

condition and is evaluated according to the following equation [41]:

$$Precision = \left(1 - \left|\frac{F_i - F_\mu}{F_\mu}\right|\right)100\% \quad (11)$$

where F_i is the average strain value measured from 52 to 78 s for the ith experiment for one loading state of the sensor, and F_μ is the average strain for all sets of experiments for the same loading condition. In this work, three experiments were performed for each loading condition.

Fig. 10 shows representative sensor data for three experiments with the same applied displacement. The precision values for all the controlled displacement experiments (21–315 μm) were determined using (11).

The strain gauge-based sensor consistently demonstrated a high precision ($\geq 87.22\%$) for all displacements except the first two (21 and 42 μm). The low precision for these smaller displacements could be attributed to frictional energy losses between the sensor head legs and sensor base slot feature.

E. Repeatability

Repeatability pertains to the level of consistency exhibited for multiple measurements obtained from a sensor or measurement system when subjected to identical input conditions [31]. The repeatability of the sensor, ρ, is evaluated using (12), where ΔF_{max} is the maximum deviation across all sets of experiments, and F_R is the range of force measurement [31]

$$\rho = \pm\left(\frac{\Delta F_{max}}{F_R}\right) \times 100\%. \quad (12)$$

Fig. 11 presents the deviation in force (evaluated from measured strain gauge data) between the three experiments for each loading condition. Based on experimental results presented in Fig. 11, $\Delta F_{max} = 0.025$ N and $F_r = 0.87$ N yield a repeatability of $\pm 2.87\%$ according to (12).
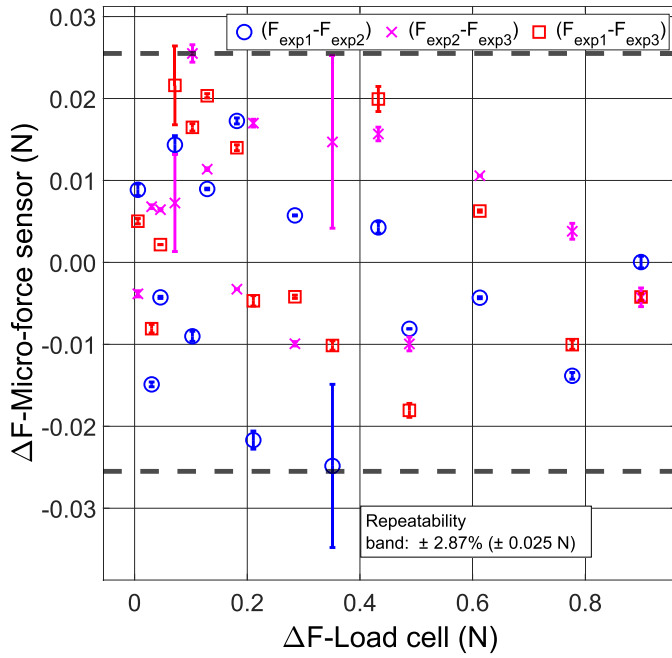
Fig. 11. Sensor force repeatability band evaluated from measured change in resistance in triplicate for each loading condition.
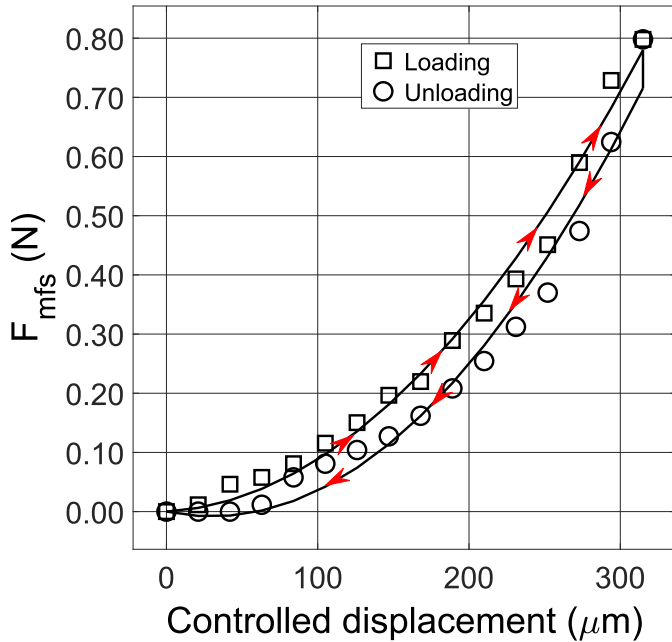

Fig. 12. Post-processed hysteresis response from the calibrated micro-force sensor.

F. Hysteresis

Hysteresis is the phenomenon where changes in the value of a physical attribute lag behind changes in the effect causing them [44]. The largest deviation between the loading and unloading of the micro-force sensor over its defined operational range is used to assess hysteresis as a performance metric. The hysteresis is evaluated according to (13), where $F_{loading}$ and $F_{unloading}$ represent the calculated force during loading and unloading, respectively [44]

$$\psi = \text{Max}\left| F_{loading} - F_{unloading} \right|. \qquad (13)$$

TABLE II
PERFORMANCE MATRIX OF THE PROTOTYPED MICRO-FORCE SENSOR

Characteristic	Specification
Diameter	3.3 mm (sensor housing)
Force Range	0-0.87 N (normal force)
Sensitivity	859.7 $\mu\epsilon$/N
Resolution	2.6 mN
Accuracy	$\pm$ 28.6 mN
Precision	87.22%
Repeatability band	$\pm$ 2.87%

Hysteresis losses were estimated by subjecting the sensor to incremental loading intervals and allowing the sensor to reach a steady state for each increment until the maximum displacement was reached. Then, the unloading profile followed a decrement from the maximum displacement at predefined intervals while allowing the sensor to reach steady state until the initial zero displacement. Fig. 12 presents the post-processed hysteresis data from the micro-force sensor.

As the input displacement increases, the sensor response increases and provides a measurable output at the defined displacement. Using (13), a maximum hysteresis of 118 mN was calculated at a displacement of 273 μm. The hysteresis losses recorded from the sensor characterization experiments demonstrated that the assembled sensor releases energy during the unloading phase. The hysteresis losses of the micro-force sensor could be attributed to multiple factors including the friction between the sensor head leg feature and the sensor base guide slots.

G. Performance Matrix Summary

The performance characteristics of the prototyped micro-force sensor based on the experimentally obtained and processed measurements are summarized in Table II. These results demonstrate that the micro-force sensor met the desired design specifications (see Table I) for its intended application in obtaining tissue relaxation responses during tissue palpation in confined spaces.

V. CONCLUSION

This manuscript introduced a strain gauge-based uniaxial micro-force sensor aimed to be attached on a robotic manipulator for transurethral palpation of the interior of the bladder wall. The need for the micro-force sensor arises from the lack of intervention tools for the quantitative characterization of localized viscoelastic properties of soft tissue through direct palpation to improve disease prognosis. The design specifications of the micro-force sensor were established and a conceptual sensor design was presented. The performance of the sensor depends on the materials used and geometric constraints based on the intended application, and as such a design optimization problem was formulated. The optimal design parameters of the sensing element were defined and evaluated through a discrete exhaustive search approach using FE analysis. The design parameters values guided the fabrication of a functional prototype of the micro-force sensor.

The performance of the prototyped sensor was experimentally characterized through a number of experiments using a custom-developed testbed. The theoretical and experimental analyses show a high agreement between them confirming the procedures followed for analysis and characterization. The results from the characterization experiments demonstrated an accuracy of 28.6 mN, a precision of 87.22%, a resolution of 2.6 mN, a sensitivity of 859.73 $\mu\epsilon$/N, and a repeatability band of $\pm2.87\%$. The controlled displacement hysteresis was evaluated to be 118 mN. These sensor performance results reinforce continuing research toward employing the micro-force sensor to characterize viscoelastic properties of soft tissue in vivo.

ACKNOWLEDGMENT

REFERENCES

[1] J. Guo, B. Xiao, and H. Ren, "Compensating uncertainties in force sensing for robotic-assisted palpation," *Appl. Sci.*, vol. 9, no. 12, p. 2573, Jun. 2019. [Online]. Available: https://www.mdpi.com/2076-3417/9/12/2573

[2] H. Benzon, S. Fishman, S. Liu, S. P. Cohen, and S. N. Raja, *Essentials of Pain Medicine*. Amsterdam, The Netherlands: Elsevier, 2011. [Online]. Available: https://linkinghub.elsevier.com/retrieve/pii/C20090610783

[3] G. Bigley, "Proprioceptive sensation," in *Clinical Methods: The History, Physical, and Laboratory Examinations*. Boston, MA, USA: Butterworths, 1990, pp. 343–350.

[4] S. Maharjan et al., "Directional filter, local frequency estimate and algebraic inversion of differential equation of psoas major magnetic resonance elastography," *Open J. Med. Imag.*, vol. 10, no. 1, pp. 1–16, 2020. [Online]. Available: https://www.scirp.org/journal/doi.aspx?doi=10.4236/ojmi.2020.101001

[5] M. Moeinzadeh, S. Davaria, F. Najafi, and M. Haghighi, "Design and fabrication of a portable 1-DOF robotic device for indentation tests," *J. Comput. Appl. Mech.*, vol. 49, no. 1, pp. 179–188, 2018. [Online]. Available: https://jcamech.ut.ac.ir/article_63272.html

[6] D. P. Byar and F. K. Mostofi, "Carcinoma of the prostate: Prognostic evaluation of certain pathologic features in 208 radical prostatectomies," *Cancer*, vol. 30, no. 1, pp. 5–13, Jul. 1972. [Online]. Available: https://pubmed.ncbi.nlm.nih.gov/5064808/

[7] B. Qiang, J. Greenleaf, M. Oyen, and X. Zhang, "Estimating material elasticity by spherical indentation load-relaxation tests on viscoelastic samples of finite thickness," *IEEE Trans. Ultrason., Ferroelectr., Freq. Control*, vol. 58, no. 7, pp. 1418–1429, Jul. 2011. [Online]. Available: http://ieeexplore.ieee.org/document/5953997/

[8] C. N. Wang, M. R. Abraham, C. E. Abrego, P. S. Shiakolas, A. Christie, and P. E. Zimmern, "An operator-independent artificial finger can differentiate anterior vaginal wall indentation parameters between control and prolapse patients," *J. Biomechanics*, vol. 120, May 2021, Art. no. 110378, doi: 10.1016/j.jbiomech.2021.110378. [Online]. Available: https://linkinghub.elsevier.com/retrieve/pii/S0021929021001585

[9] B. Ahn, Y. Kim, and J. Kim, "New approach for abnormal tissue localization with robotic palpation and mechanical property characterization," in *Proc. IEEE/RSJ Int. Conf. Intell. Robots Syst.*, Sep. 2011, pp. 4516–4521. [Online]. Available: http://ieeexplore.ieee.org/document/6094786/

[10] C. Lv, S. Wang, and C. Shi, "A high-precision and miniature fiber Bragg grating-based force sensor for tissue palpation during minimally invasive surgery," *Ann. Biomed. Eng.*, vol. 48, no. 2, pp. 669–681, Feb. 2020. [Online]. Available: http://link.springer.com/10.1007/s10439-019-02388-w

[11] A. Ansardamavandi, M. Tafazzoli-Shadpour, R. Omidvar, and I. Jahanzad, "Quantification of effects of cancer on elastic properties of breast tissue by atomic force microscopy," *J. Mech. Behav. Biomed. Mater.*, vol. 60, pp. 234–242, Jul. 2016. [Online]. Available: https://linkinghub.elsevier.com/retrieve/pii/S1751616115005020

[12] P. Saccomandi, E. Schena, C. Oddo, L. Zollo, S. Silvestri, and E. Guglielmelli, "Microfabricated tactile sensors for biomedical applications: A review," *Biosensors*, vol. 4, no. 4, pp. 422–448, Nov. 2014. [Online]. Available: http://www.mdpi.com/2079-6374/4/4/422

[13] H. H. Ly, Y. Tanaka, and M. Fujiwara, "Tumor depth and size perception using a pneumatic tactile display in laparoscopic surgery," *IEEE Access*, vol. 9, pp. 167795–167811, 2021. [Online]. Available: https://ieeexplore.ieee.org/document/9650891/

[14] M. Tanimoto et al., "Micro force sensor for intravascular neuro-surgery and in vivo experiment," in *Proc. IEEE 11th Annu. Int. Workshop Micro Electro Mech. Systems. Invest. Micro Struct., Sensors, Actuat., Mach. Syst.*, Jan. 1998, pp. 504–509. [Online]. Available: http://ieeexplore.ieee.org/document/659809/

[15] D. Shin, H.-U. Kim, A. Kulkarni, Y.-H. Kim, and T. Kim, "Development of force sensor system based on tri-axial fiber Bragg grating with flexure structure," *Sensors*, vol. 22, no. 1, p. 16, Dec. 2021. [Online]. Available: https://www.mdpi.com/1424-8220/22/1/16

[16] B. Alekya, V. S. N. Sitaramgupta, B. S. Arjun, and H. J. Pandya, "Sensor for meso-scale tissue stiffness characterization," *IEEE Sensors J.*, vol. 22, no. 7, pp. 6442–6453, Apr. 2022. [Online]. Available: https://ieeexplore.ieee.org/document/9721234/

[17] S. S. Kumat and P. S. Shiakolas, "Design, inverted vat photopolymerization 3D printing, and initial characterization of a miniature force sensor for localized in vivo tissue measurements," *3D Printing Med.*, vol. 8, no. 1, p. 1, Dec. 2022. [Online]. Available: https://threedmedprint.biomedcentral.com/articles/10.1186/s41205-021-00128-2

[18] T. Li, A. Pan, and H. Ren, "A high-resolution triaxial catheter tip force sensor with miniature flexure and suspended optical fibers," *IEEE Trans. Ind. Electron.*, vol. 67, no. 6, pp. 5101–5111, Jun. 2020. [Online]. Available: https://ieeexplore.ieee.org/document/8766123/

[19] F. J. Carter, T. G. Frank, P. J. Davies, D. McLean, and A. Cuschieri, "Measurements and modelling of the compliance of human and porcine organs," *Med. Image Anal.*, vol. 5, no. 4, pp. 231–236, Dec. 2001. [Online]. Available: https://linkinghub.elsevier.com/retrieve/pii/S1361841501000482

[20] E. Samur, M. Sedef, C. Basdogan, L. Avtan, and O. Duzgun, "A robotic indenter for minimally invasive measurement and characterization of soft tissue response," *Med. Image Anal.*, vol. 11, no. 4, pp. 361–373, Aug. 2007. [Online]. Available: https://linkinghub.elsevier.com/retrieve/pii/S136184150700031X

[21] M. C. Yip, S. G. Yuen, and R. D. Howe, "A robust uniaxial force sensor for minimally invasive surgery," *IEEE Trans. Biomed. Eng.*, vol. 57, no. 5, pp. 1008–1011, May 2010. [Online]. Available: http://ieeexplore.ieee.org/document/5415630/

[22] P. Puangmali, H. Liu, L. D. Seneviratne, P. Dasgupta, and K. Althoefer, "Miniature 3-axis distal force sensor for minimally invasive surgical palpation," *IEEE/ASME Trans. Mechatronics*, vol. 17, no. 4, pp. 646–656, Aug. 2012. [Online]. Available: http://ieeexplore.ieee.org/document/5732701/

[23] B. Luo, Y. Deng, T. Yang, S. Dai, and G. Song, "Design of a miniature fiber optic sensor to measure axial force at the tip of a robotic flexible ureteroscope," in *Proc. Chin. Autom. Congr. (CAC)*, Nov. 2019, pp. 2554–2559. [Online]. Available: https://ieeexplore.ieee.org/document/8996395/

[24] N. Kumar, O. Piccin, L. Meylheuc, L. Barbé, and B. Bayle, "Design and modeling of a polymer force sensor," *IEEE/ASME Trans. Mechatronics*, vol. 21, no. 1, pp. 555–564, Feb. 2016. [Online]. Available: http://ieeexplore.ieee.org/document/7131564/

[25] S. Standring, *The Anatomical Basis of Clinical Practice*, S. Standring, Eds. London, U.K.: Jeremy Bowes, 2016.

[26] G. S. Bhat, M. Shivalingaiah, G. G. Nelivigi, and C. Ratkal, "The size of external urethral meatus on maximum stretch in Indian adult males," *Indian J. Surg.*, vol. 76, no. 1, pp. 85–89, Feb. 2014. [Online]. Available: http://link.springer.com/10.1007/s12262-012-0549-x

[27] C. D. Berry, "Urethral meatal caliber in circumcised and uncircumcised males," *Arch. Pediatrics Adolescent Med.*, vol. 92, no. 2, p. 152, Aug. 1956, doi: 10.1001/archpedi.1956.02060030146007.

[28] R. G. Hudson, M. J. Conlin, and D. H. Bagley, "Ureteric access with flexible ureteroscopes: Effect of the size of the ureteroscope," *BJU Int.*, vol. 95, no. 7, pp. 1043–1044, May 2005. [Online]. Available: https://onlinelibrary.wiley.com/doi/10.1111/j.1464-410X.2005.05462.x

[29] A. Miernik, K. Wilhelm, P. U. Ardelt, F. Adams, F. E. Kuehhas, and M. Schoenthaler, "Standardized flexible ureteroscopic technique to improve stone-free rates," *Urology*, vol. 80, no. 6, pp. 1198–1202, Dec. 2012.

[30] S. K. Lildal, K. H. Andreassen, H. Jung, M. R. Pedersen, and P. J. S. Osther, "Evaluation of ureteral lesions in ureterorenoscopy: Impact of access sheath use," *Scandin. J. Urol.*, vol. 52, no. 2, pp. 157–161, Mar. 2018.

[31] Y. Deng, T. Yang, S. Dai, and G. Song, "A miniature triaxial fiber optic force sensor for flexible ureteroscopy," *IEEE Trans. Biomed. Eng.*, vol. 68, no. 8, pp. 2339–2347, Aug. 2021. [Online]. Available: https://ieeexplore.ieee.org/document/9242290/

[32] V. De Coninck et al., "Complications of ureteroscopy: A complete overview," *World J. Urology*, vol. 38, no. 9, pp. 2147–2166, Sep. 2020, doi: 10.1007/s00345-019-03012-1. [Online]. Available: http://link.springer.com/10.1007/s00345-019-03012-1

[33] S. A. Adejokun and P. S. Shiakolas, "A compliant manipulator for confined space tissue diagnostics: Kinematic and force analyses and initial characterization experiments," *J. Mech. Robot.*, vol. 16, no. 2, pp. 1–23, Feb. 2024, doi: 10.1115/1.4062762/1164053.

[34] S. A. Adejokun, S. S. Kumat, and P. S. Shiakolas, "A microrobot with an attached micro-force sensor for natural orifice access to the bladder interior wall," in *Proc. Biomed. Biotechnol. Des. Syst. Complex.*, vol. 4, Columbus, OH, USA, Oct. 2022, Paper no. V004T05A065. [Online]. Available: https://asmedigitalcollection.asme.org/IMECE/proceedings/IMECE2022/86663/V004T05A065/1157016, doi: 10.1115/IMECE2022-95988.

[35] S. A. Adejokun, S. S. Kumat, and P. S. Shiakolas, "A microrobot with an attached microforce sensor for transurethral access to the bladder interior wall," *J. Eng. Sci. Med. Diag. Therapy*, vol. 6, no. 3, pp. 1–29, Aug. 2023. [Online]. Available: https://asmedigitalcollection.asme.org/medicaldiagnostics/article/6/3/031001/1157527/A-Microrobot-With-an-Attached-Microforce-Sensor

[36] C. A. Duarte, I. Babuška, and J. T. Oden, "Generalized finite element methods for three-dimensional structural mechanics problems," *Comput. Struct.*, vol. 77, no. 2, pp. 215–232, Jun. 2000. [Online]. Available: https://linkinghub.elsevier.com/retrieve/pii/S0045794999002114

[37] R. L. Norton, *Machine Design: An Integrated Approach*, 4th ed. Worcester, MA, USA: Pearson Education, 2010.

[38] S. Kalpakjian, *Manufacturing Engineering and Technology* (Computer Engineering). Reading, MA, USA: Addison-Wesley, 1989. [Online]. Available: https://books.google.com/books?id=Pht2QgAACAAJ

[39] National Instruments. (2023). *NI-9219 Specifications*. [Online]. Available: https://www.ni.com/docs/en-U.S./bundle/ni-9219-specs/page/specs.html

[40] Acromag. (2019). *Strain Gauge & Load Cell Input Transmitters Whitepaper: Introduction to Strain & Strain Measurement*. [Online]. Available: https://www.acromag.com/wp-content/uploads/2019/10/White-Paper-Intro-StrainGauge

[41] M. Haddad and C. Regier, "Demystifying instrument specifications—How to make sense out of the Jargon," Dept. Networked Syst. Services, Nat. Instrum., Austin, TX, USA, Appl. Note 152, Dec. 2000. [Online]. Available: http://www.hit.bme.hu/

[42] A. R. Ahmad, T. Wynn, and C.-Y. Lin, "A comprehensive design of six-axis force/moment sensor," *Sensors*, vol. 21, no. 13, p. 4498, Jun. 2021. [Online]. Available: https://www.mdpi.com/1424-8220/21/13/4498

[43] Y. B. Kim et al., "6-axis force/torque sensor with a novel autonomous weight compensating capability for robotic applications," *IEEE Robot. Autom. Lett.*, vol. 5, no. 4, pp. 6686–6693, Oct. 2020. [Online]. Available: https://ieeexplore.ieee.org/document/9165165/

[44] J. J. Carr, *Introduction to Biomedical Equipment Technology*. London, U.K.: Pearson Education, 2001.

Shashank S. Kumat received the Bachelor of Engineering degree from the University of Pune, Pune, India, in 2013, and the M.S. and Ph.D. degrees in mechanical engineering from The University of Texas at Arlington, Arlington, TX, USA, in 2016 and 2023, respectively.

He was a Research Assistant at the Center for the Integration of Research, Teaching and Learning (CIRTL), The University of Texas at Arlington, where he assisted in organizing and conducting events providing graduate students with tools to learn and teach in STEM majors. He is a Mechanical Engineer at Thorlabs Inc., Newton, NJ, USA. His research interests include medical robotics, additive manufacturing, and system design and integration.

Panos S. Shiakolas received the Higher National Diploma degree from the Higher Technical Institute, Nicosia, Cyprus, in 1982, the B.S. and M.S. degrees from the University of Texas at Austin, Austin, TX, USA, in 1986 and 1988, respectively, and the Ph.D. degree from The University of Texas at Arlington, Arlington, in 1992, all in mechanical engineering in the areas of robotic automation and computer-aided design.

He was a Faculty-Research Associate at The University of Texas at Arlington, from 1993 to 1996. He was with the Cypriot National Guard, Nicosia, as a Non-Commissioned Sergeant and a Honorably Discharged, in 1984. He joined the Faculty as an Assistant Professor in 1996, and is currently a Tenured Associate Professor of Mechanical and Aerospace Engineering at The University of Texas at Arlington. His research interests are in the areas of robotics, medical devices, manufacturing, micro-systems, automation, and controls as they apply to the betterment of society along, with his passion for engineering education.